

# Decoding Li<sup>+</sup>/Na<sup>+</sup> Exchange Route Toward High-Performance Mn-Based Layered Cathodes for Li-Ion Batteries

Bo Cao, Zhefeng Chen, Hongbin Cao, Chen Zhu, Hongkai Yang, Tianyi Li,\* Wenqian Xu, Feng Pan,\* and Mingjian Zhang\*

Li<sup>+</sup>/Na<sup>+</sup> exchange has been extensively explored as an effective method to prepare high-performance Mn-based layered cathodes for Li-ion batteries, since the first report in 1996 by P. G. Bruce (Nature, 1996. 381, 499-500). Understanding the detailed structural changes during the ion-exchange process is crucial to implement the synthetic control of high-performance layered Mn-based cathodes, but less studied. Herein, in situ synchrotron X-ray diffraction, density functional theory calculations, and electrochemical tests are combined to conduct the systemic studies into the structural changes during the ion-exchange process of an Mn-only layered cathode O3-type Li<sub>0.67</sub>[Li<sub>0.22</sub>Mn<sub>0.78</sub>]O<sub>2</sub> (LLMO) from the corresponding counterpart P3-type Na<sub>0.67</sub>[Li<sub>0.22</sub>Mn<sub>0.78</sub>]O<sub>2</sub> (NLMO). The temperature-resolved observations combined with theoretical calculations reveal that the Li<sup>+</sup>/Na<sup>+</sup> exchange is favorable thermodynamically and composited with two tandem topotactic phase transitions: 1) from NLMO to a layered intermediate through ≈60% of Li<sup>+</sup>/Na<sup>+</sup> exchange. 2) then to the final layered product LLMO through further Li insertion. Moreover, the intermediate-dominate composite is obtained by slowing down the exchange kinetics below room temperature, showing better electrochemical performance than LLMO obtained by the traditional moltensalt method. The findings provide guides for the synthetic control of highperformance Mn-based cathodes under mild conditions.

1. Introduction

Layered Mn-based oxides are considered as promising cathodes due to their low cost and high energy density.<sup>[1]</sup> Conventional

B. Cao, Z. Chen, H. Cao, C. Zhu, H. Yang, F. Pan School of Advanced Materials Peking University Shenzhen Graduate School Shenzhen 518055, China E-mail: panfeng@pkusz.edu.cn T. Li, W. Xu X-ray Science Division Advanced Photon Source Argonne National Laboratory Lemont, IL 60439, USA E-mail: tianyi.li@anl.gov M. Zhang

School of Science and Engineering The Chinese University of Hong Kong Shenzhen 518172, China E-mail: zhangmingjian@cuhk.edu.cn

The ORCID identification number(s) for the author(s) of this article can be found under https://doi.org/10.1002/adfm.202214921.

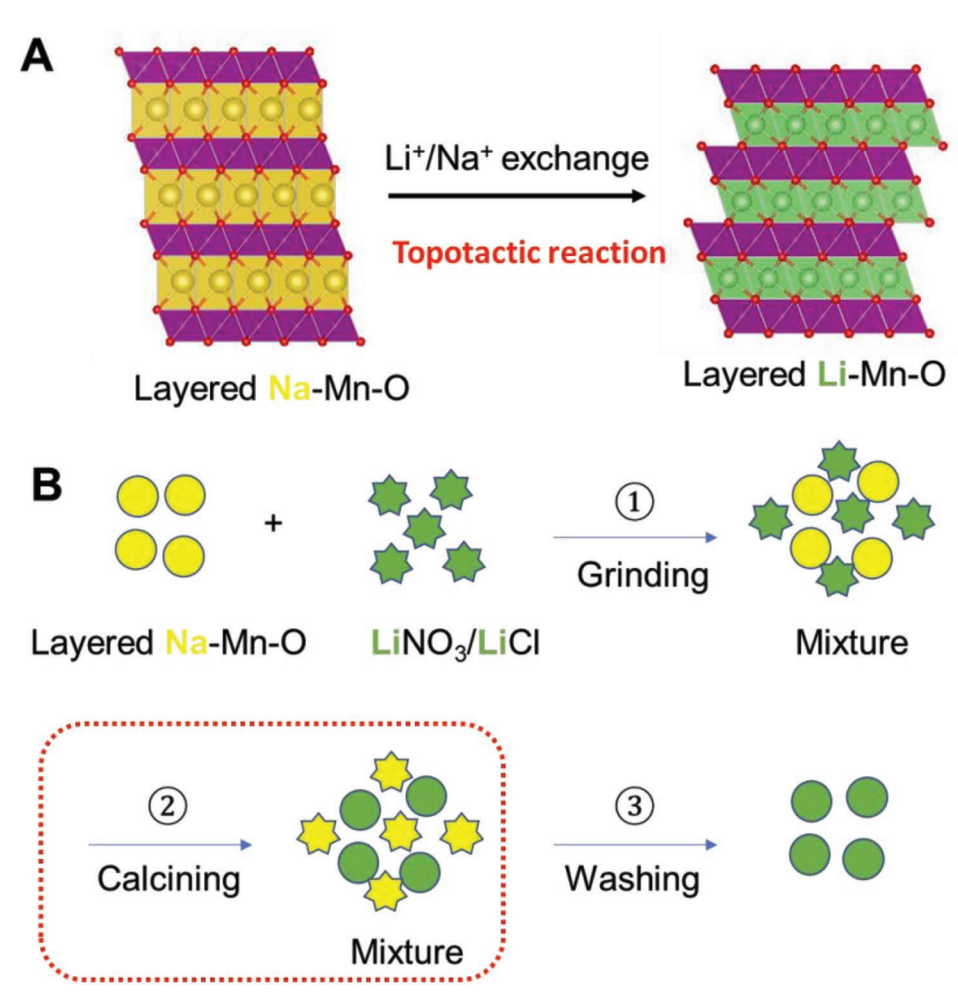
DOI: 10.1002/adfm.202214921

methods to synthesize lithium-rich Mnbased layered oxides include solid-state method,[2] sol-gel method,[3] and coprecipitation method.[4] As a non-conventional method, The ion-exchange method has a unique advantage in preparing thermodynamically meta-stable phases, which cannot be obtained by conventional methods. The stoichiometric layered LiMnO2 cannot be obtained through the conventional methods due to its thermodynamically metastable nature.<sup>[5]</sup> In 1996, P. G. Bruce et al. reported the first synthesis of O3-type layered LiMnO<sub>2</sub> from the counterpart NaMnO2 through a unique Li+/Na+ exchange method using the n-hexanol solution of LiCl/LiBr.[6] Ten years later (2006), Ceder group modified the ion-exchange method to synthesize an O3-type layered Li(Ni<sub>0.5</sub>Mn<sub>0.5</sub>) O2 with reduced intralayer Li/Ni mixing using LiNO<sub>3</sub>/LiCl as the high-temperature eutectic molten salt.[7] Nevertheless. the modified ion-exchange method was applied to the synthesis of a series of highperformance layered Mn-based cathodes

until recently. In 2018, Dingguo Xia group prepared an O2/ O4-hybrid layered Li<sub>1.25</sub>Co<sub>0.25</sub>Mn<sub>0.5</sub>O<sub>2</sub> cathode with the singlelayer Li<sub>2</sub>MnO<sub>3</sub> superstructure through ion-exchange route, showing an ultrahigh reversible capacity of 400 mA h g-1.[8] In 2020, Haoshen Zhou group reported an O3-type layered Li<sub>0.6</sub>[Li<sub>0.2</sub>Mn<sub>0.8</sub>]O<sub>2</sub> cathode through ion-exchange route from a P3-type Na-containing precursor Na<sub>0.6</sub>[Li<sub>0.2</sub>Mn<sub>0.8</sub>]O<sub>2</sub>, which exhibited stable anionic redox chemistry and the improved cycling stability.<sup>[9]</sup> Similarly, Dingguo Xia group reported another O3-type layered  $Li_{0.700}[Li_{0.222}Mn_{0.756}]O_2$  cathode through ion-exchange route, delivering a reversible capacity of over 300 mA h g<sup>-1</sup>.[10] In the same year, Eum et al. obtained O2-type layered  $Li_x[Li_{0.2}Ni_{0.2}Mn_{0.6}]O_2$  cathodes through the ion-exchange process from a P2-type Na-containing precursor, and proposed the critical role of the O2-type oxygen stacking sequence in improving the reversibility of cation migration and thus reducing voltage decay.[11] In addition, ion exchange was also applied to the synthesis of other layered oxides, such as Li<sub>2</sub>RhO<sub>3</sub>.<sup>[12]</sup> All these works were focused on the unique layered structures with the diverse forms of oxygen stacking arrangement (O2, O3, O2-O4 hybrid, etc.) and the enhanced electrochemistry, while discussing less on the complex ion-exchange

16163028, 2023, 20, Downloaded from https://advanced.onlinelibrary.wiley.com/doi/10.1002/adfm.202214921 by University Town Of Shenzhen, Wiley Online Library on [23/11/2025]. See the Terms

-conditions) on Wiley Online Library for rules of use; OA articles are governed by the applicable Creative Commons License



Scheme 1. A) The ion-exchange route to prepare the thermodynamically metastable layered Li—Mn—O phase based on the topotactic reaction. B) The typical synthesis process for the molten salt ion-exchange route contains three steps: grinding, calcining, and washing.

process involving the different Li/Na exchange extents and the induced structural changes.  $^{[13]}$ 

Figuring out the detailed structural changes in the ionexchange process is crucial to implement the synthetic control of these high-performance layered Mn-based cathodes. Here taking the widely used molten salt method as an example, the synthetic process is analyzed in detail. Scheme 1 shows a typical modified ion-exchange process. Na-containing layered precursor (Na-Mn-O) is pre-synthesized through traditional solidstate methods or sol-gel method, then transforms to the final Li-containing layered cathode (Li-Mn-O) through a topotactic reaction via Li+/Na+ exchange (Scheme 1A). The experimental process contains three steps (Scheme 1B): ① mixing Na-Mn-O and the eutectic molten salt (LiNO<sub>3</sub>/LiCl, 88/12 wt./wt.) thoroughly by grinding or ball milling; 2 Calcining the mixture, usually at 280 °C for several hours; 3 Washing away the water-soluble salts (LiNO3, LiCl, NaNO3, NaCl, etc.) to obtain the product Li-Mn-O. Generally, it is considered the Li<sup>+</sup>/Na<sup>+</sup> exchange occurs during the calcination step.<sup>[14]</sup> In situ structural studies are required to further illustrate the details of structural changes in each step, for establishing the relationship between the structural changes and the ion-exchange extents under the real synthetic conditions.

In this work, we employed the temperature-resolved synchrotron XRD to track the Li<sup>+</sup>/Na<sup>+</sup> exchange process and the induced structure changes during the ion-exchange reaction. Real-time observation combined with the DFT calculations revealed two tandem topotactic phase transformations, both of which are favorable thermodynamically. By tuning the synthetic kinetics, the ion-exchange was successfully conducted at room temperature and even below, producing cathodes with excellent electrochemical performance comparable to that prepared by the traditional molten salt method. The findings highlight the synthetic control of ion-exchange kinetics to obtain high-performance layered Mn-based cathodes.

# 2. Results and Discussion

# 2.1. Li<sup>+</sup>/Na<sup>+</sup> Exchange During Calcination

To study the structural changes during the heating process, temperature-resolved high-energy XRD patterns were collected on the mixture of Na-containing precursor P3-type  $Na_{0.67}Li_{0.22}Mn_{0.78}O_2$  (NLMO) and the eutectic molten salt (see details in experimental section). All XRD patterns are

www.advancedsciencenews.com

www.afm-journal.de

16163028, 2023, 20, Downloaded from https://advanced.onlinelibrary.wiley.com/doi/10.1002/adfm.202214921 by University Town Of Shenzhen, Wiley Online Library on [23/11/2025]. See the Terms and Conditions (https://advanced.onlinelibrary.wiley.com/doi/10.1002/adfm.202214921 by University Town Of Shenzhen, Wiley Online Library on [23/11/2025]. See the Terms and Conditions (https://advanced.onlinelibrary.wiley.com/doi/10.1002/adfm.202214921 by University Town Of Shenzhen, Wiley Online Library on [23/11/2025]. See the Terms and Conditions (https://advanced.onlinelibrary.wiley.com/doi/10.1002/adfm.202214921 by University Town Of Shenzhen, Wiley Online Library on [23/11/2025]. See the Terms and Conditions (https://advanced.onlinelibrary.wiley.com/doi/10.1002/adfm.202214921 by University Town Of Shenzhen, Wiley Online Library on [23/11/2025]. See the Terms and Conditions (https://advanced.onlinelibrary.wiley.com/doi/10.1002/adfm.202214921 by University Town Of Shenzhen, Wiley Online Library on [23/11/2025]. See the Terms and Conditions (https://advanced.onlinelibrary.wiley.com/doi/10.1002/adfm.202214921 by University Town Of Shenzhen, Wiley Online Library on [23/11/2025]. See the Terms and Conditions (https://advanced.onlinelibrary.wiley.com/doi/10.1002/adfm.202214921 by University Town Of Shenzhen, Wiley Online Library on [23/11/2025]. See the Terms and Conditions (https://advanced.onlinelibrary.wiley.com/doi/10.1002/adfm.202214921 by University Town Of Shenzhen, Wiley Online Library on [23/11/2025]. See the Terms and Conditions (https://advanced.onlinelibrary.wiley.com/doi/10.1002/adfm.202214921 by University Town Of Shenzhen, Wiley Online Library on [23/11/2025]. See the Terms and Conditions (https://advanced.onlinelibrary.wiley.com/doi/10.1002/adfm.202214921 by University Town Of Shenzhen, Wiley Online Library on [23/11/2025]. See the Terms and Conditions (https://advanced.onlinelibrary.wiley.com/doi/10.1002/adfm.202214921 by University Town Online Library (https://advanced.onlinelibrary.wiley.com/doi/10.1002/adfm.2

onditions) on Wiley Online Library for rules of use; OA articles are governed by the applicable Creative Commons License

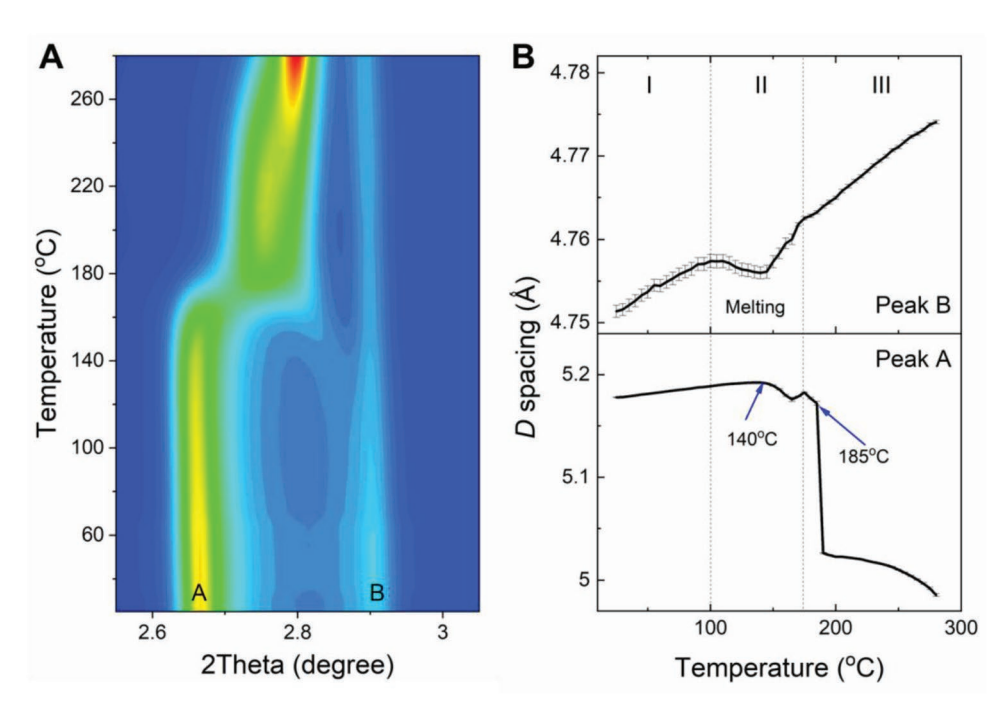


Figure 1. A) The contour plot of in situ XRD data during the calcination in the region of 2.5–3.1 degrees. Peaks A and B represent the main peak of Na-containing precursor and tiny  $\text{Li}_2\text{MnO}_3$  impurity. B) The peak positions of peaks A and B as a function of the temperature to track the phase transition during the calcination.

shown in Figure S1 (Supporting Information). Several patterns at different temperatures are plotted in Figure S2 (Supporting Information). It is clear that the whole patterns undergo great changes with the temperature, especially at  $\approx\!160$  °C, hinting the phase transformation occurred during heating. In addition, the characteristic peaks of NaNO3 and NaCl can be observed, reflecting the progress of ion-exchange reaction.

To track the detailed phase transformation process, the region containing the main peaks (marked by the rectangle in Figure S1, Supporting Information) was enlarged in Figure 1A. Two peaks before heating, A and B, can be ascribed to the Nacontaining precursor and a small amount of Li<sub>2</sub>MnO<sub>3</sub> purity (due to the excess Li source), respectively. As the temperature increases, Peak A linearly shifts to the lower angle due to the lattice expansion, and then undergoes an abrupt and big shift to the higher angle at ≈160 °C, hinting a swift phase transformation. Peak B from the tiny Li<sub>2</sub>MnO<sub>3</sub> seems to linearly shift to the lower angle with the temperature increase, which can act as an ideal benchmark for the environmental temperature/condition. The quantitative analysis of the peak shift was performed using multiple peak fittings. As shown in Figure 1B, the whole heating process can be roughly divided into three sections according to the peak shift of Peak B, Section I (RT-100 °C), II (100–175 °C), and III (>175 °C). The d spacing of Peak B linearly increases in Region I and III, while undergoing a little drop and then an increase in Region II. The thermal expansion coefficients in Region I and III are different,  $8.35 \times 10^{-5}$  and  $1.15 \times 10^{-4} \text{ Å} \, ^{\circ}\text{C}^{-1}$ , respectively. Considering that Li<sub>2</sub>MnO<sub>3</sub> does not participate in the ion exchange reaction and just reflects the change of sample environment, we can deduce that, the eutectic molten salt undergoes a melting process in Region II, which alters the sample environment and thus the thermal expansion coefficient of Li<sub>2</sub>MnO<sub>3</sub>. The d spacing of Peak A starts to decrease a little ( $\approx$ 0.02 Å) from 140 °C in Region II and experiences a great decrease from 5.16 to 5.025 Å at  $\approx$ 185 °C in Region III. It indicates that the fast ion-exchange can be activated in the molten salt, which induces the abrupt phase transformation. After the phase transformation, the d spacing of the new-formed layered phase continues decreasing gradually with the temperature, and the holding time (Figures S3 and S4, Supporting Information), hinting that further ion-exchange or cationic rearrangement occurred in the layered phase. [14,15] Finally, a stable d spacing of  $\approx$ 4.91 Å is obtained after holding at 280 °C for  $\approx$ 0.5 h (Figure S4B, Supporting Information), indicating the completion of the ion-exchange reaction. After cooling to room temperature, the d spacing decreases to 4.88 Å (Figure S5, Supporting Information).

#### 2.2. Li<sup>+</sup>/Na<sup>+</sup> Exchange at Room Temperature

According to the in situ XRD results above, we notice a strange phenomenon: the mixture before heating shows an interlayer spacing of 5.16 Å, much smaller than that of the P3-type Nacontaining precursor (NLMO, 5.55 Å). It hints that the ion-exchange may initiate when grinding at room temperature, inducing a big phase transformation and producing a layered intermediate phase before heating.

To validate this deduction, a series of XRD patterns were collected on the mixture of NLMO and the salts after low-speed ball-milling (200 rpm) at room temperature for different times (Figure S6, Supporting Information; Figure 2A). In Figure 2A, the main peak of NLMO at  $\approx$ 16 degrees continuously attenuates with grinding, while the main peak of LLMO at

www.advancedsciencenews.com

www.afm-journal.de

16163028, 2023. 20, Downloaded from https://advanced.onlinelibrary.wiley.com/doi/10.1002/adfm.202214921 by University Town Of Shenzhen, Wiley Online Library on [23/11/2025]. See the Terms and Conditions (https://onlinelibrary.wiley.com/terms

and-conditions) on Wiley Online Library for rules of use; OA articles are governed by the applicable Creative Commons License

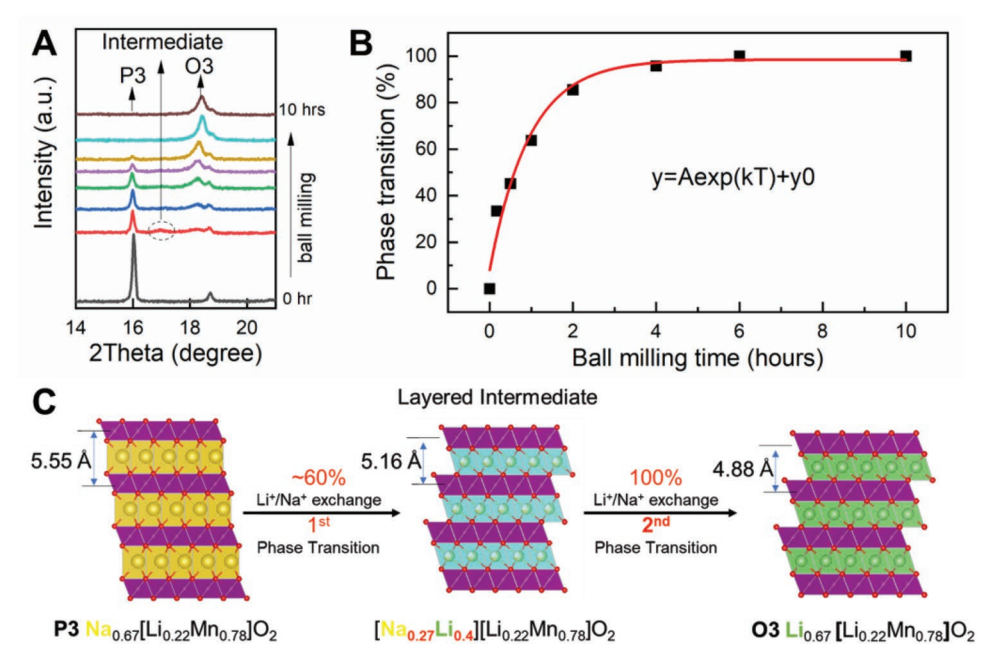


**Figure 2.** A) Ex situ XRD of the mixture of NLMO and the molten salt after ball milling for different times in the region of 14–21 degrees. B) The degree of phase transition as a function of the ball milling time. The degree of phase transition is defined as the percentage of the O3 main peak area over the total peak areas of O3 and P3 main peaks. The curve is the fitting to the data using an exponential equation  $y = A\exp(kT) + y_0$  (wherein A is the pre-exponential factor, and k is the rate coefficient). C) Schematic illustration to show the detailed structural changes, containing two topotactic phase transformations with different extents of Li<sup>+</sup>/Na<sup>+</sup> exchange.

≈18.7 degrees fast increases. After 6 h, the main peak of NLMO phase completely disappears, indicating the completion of the phase transition from P3 phase to O3 phase at room temperature. Here we can use the percentage of the peak area of the respective phase to represent the degree of the phase transition. It is plotted as a function of the time in Figure 2B. Through the exponential fitting, the rate coefficient k is determined as  $-1.05 \text{ h}^{-1}$ . [16] SEM images (Figure S7, Supporting Information) show that the final product by ball milling at room temperature (LLMO-RT) has more broken particles than LLMO obtained by the traditional molten salt method (LLMO-MS).

In addition, a small peak at  $\approx$ 17 degrees (marked by the dashed ellipse in Figure 2A) is observed after grinding for 10 minutes, corresponding to the intermediate phase observed in the in situ XRD studies above. Assume the extent of Li<sup>+</sup>/Na<sup>+</sup> exchange is proportional to the change extent of the d spacing, we can deduce that,  $\approx$ 60% of Na ions are replaced by Li ions in the intermediate phase since the final product Li<sub>0.67</sub>[Li<sub>0.22</sub>Mn<sub>0.78</sub>]O<sub>2</sub> (LLMO) has an interlayer spacing of 4.88 Å. The molecular formula of the intermediate can be deduced as [Na<sub>0.27</sub>Li<sub>0.4</sub>] [Li<sub>0.22</sub>Mn<sub>0.78</sub>]O<sub>2</sub>.

Combining the information together, the ion-exchange process can be implemented by both the traditional molten salt method and ball milling at room temperature. They experience the similar structural changes including two tandem topotactic phase transformations (Figure 2C): 1) about 60% of Li<sup>+</sup>/Na<sup>+</sup> exchange quickly proceeds and induces the first topotactic phase transformation, producing a metastable layered intermediate [Na<sub>0.27</sub>Li<sub>0.4</sub>][Li<sub>0.22</sub>Mn<sub>0.78</sub>]O<sub>2</sub>. 2) the layered intermediate undergoes the further Li<sup>+</sup>/Na<sup>+</sup> exchange, and reaches the final product LLMO through the second topotactic phase transformation.

#### 2.3. Reaction Thermodynamics by DFT Calculations

The success of Li<sup>+</sup>/Na<sup>+</sup> exchange at room temperature hints that the energy barrier for Li+/Na+ exchange may be very low, and the reaction may be favorable thermodynamically. To verify this point, we constructed the structural models of Na-containing precursor Na<sub>0.67</sub>MnO<sub>2</sub> and the Na/Li-containing precursor  $Na_{0.67}[Li_{0.22}Mn_{0.78}]O_2$ , and calculated the reaction enthalpy (ΔH) of Li+/Na+ exchange with LiCl and LiNO<sub>3</sub>, respectively (see Equations 1-4 below). Figure 3A presents the structural models for the precursors P3-type Na<sub>6</sub>Mn<sub>9</sub>O<sub>18</sub> and P3-type Na<sub>6</sub>Li<sub>2</sub>Mn<sub>7</sub>O<sub>18</sub>, and the corresponding products O3-type  $\text{Li}_6\text{Mn}_9\text{O}_{18}$  and O3-type  $\text{Li}_6\text{Li}_2\text{Mn}_7\text{O}_{18}.$  The system energies of all the species in the formula were calculated and deposited in Table S1 (Supporting Information). Accordingly, the corresponding enthalpies  $\Delta H_1$ ,  $\Delta H_2$ ,  $\Delta H_3$ , and  $\Delta H_4$  were calculated according to the reaction formulas. As shown in Figure 3B, all the entropies are negative. Considering the total molar amounts of the reactants and the products kept constant before and after the ion-exchange reaction, the reaction entropy ( $\Delta S$ ) is 0. Thus, the reaction Gibbs free energies ( $\Delta G$ ) are equal to the enthalpies ( $\Delta H$ ) in the ion-exchange reaction since  $\Delta G = \Delta H$  –  $T\Delta S$ . In addition, the configuration entropy is also considered here (see the detailed discussion below in Table S1, Supporting Information).[17] The maximum change of free energy caused by configuration entropy at room temperature is ≈30 meV, which is one order of magnitude smaller than the contribution of enthalpy (0.2–0.3 eV). Therefore, all these Li<sup>+</sup>/Na<sup>+</sup> exchange reactions are exothermic with the negative  $\Delta G$ , and thermodynamically favorable. Moreover, the reactions with LiCl release more heat than the reactions with LiNO3, and the reactions

16163028, 2023, 20, Downloaded

mlinelibrary.wiley.com/doi/10.1002/adfm.202214921 by University Town Of Shenzhen, Wiley Online Library on [23/11/2025]. See the Terms and Conditions

nditions) on Wiley Online Library for rules of use; OA articles are governed by the applicable Creative Commons

www.advancedsciencenews.com www.afm-journal.de

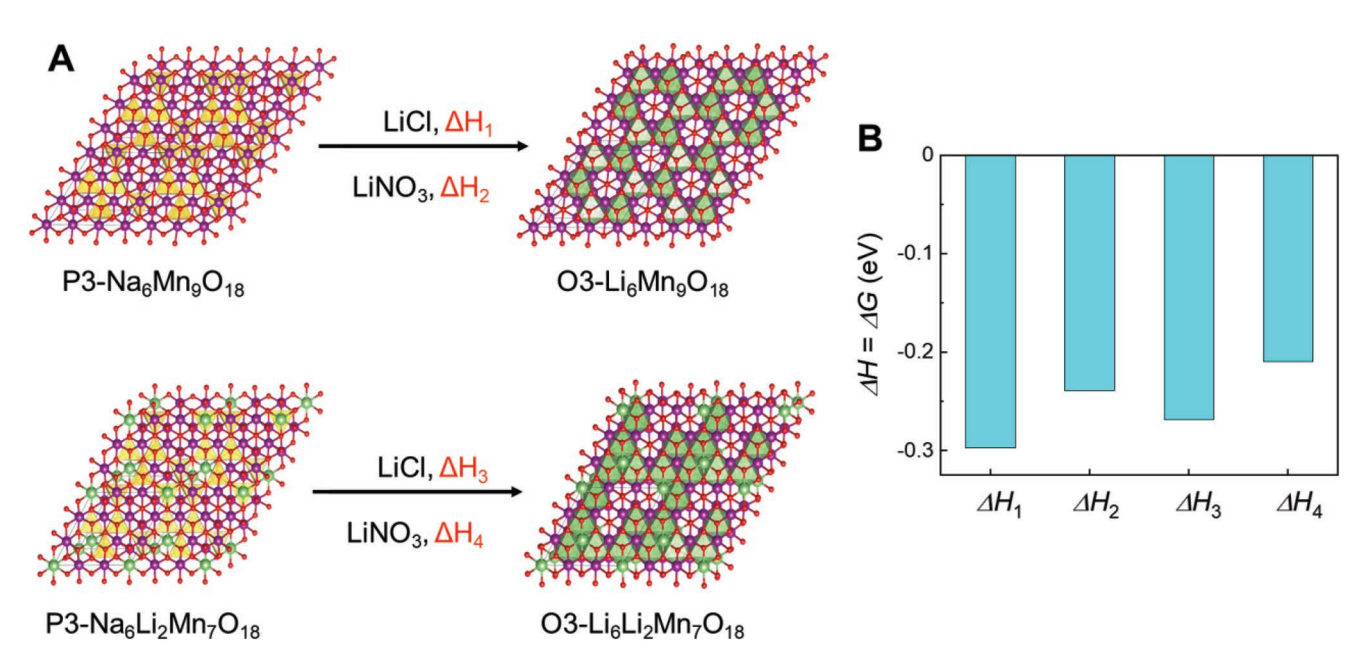


Figure 3. A) The structural models of P3-Na<sub>6</sub>Mn<sub>9</sub>O<sub>18</sub>, O3-Li<sub>6</sub>Mn<sub>9</sub>O<sub>18</sub>, P3-Na<sub>6</sub>Mn<sub>9</sub>O<sub>18</sub>, and Li<sub>6</sub>Mn<sub>9</sub>O<sub>18</sub> for DFT calculations. B) The histogram of the calculated reaction enthalpies ( $\Delta$ H).

with the Na-containing precursors release more heat than the reactions with the Li/Na-containing precursors. These theoretical results indicate that it is thermodynamically feasible to just use one kind of Li salt to complete the ion exchange at ambient conditions, consistent with our experiments above.

$$Na_{0.67}MnO_2 + 0.67 LiCl \rightarrow Li_{0.67}MnO_2 + 0.67 NaCl$$
 (1)

$$Na_{0.67}MnO_2 + 0.67 LiNO_3 \rightarrow L_{i0.67}MnO_2 + 0.67 NaNO_3$$
 (2)

$$Na_{0.67}[Li_{0.22}Mn_{0.78}]O_2 + 0.67 LiCl \rightarrow Li_{0.67}[Li_{0.22}Mn_{0.78}]O_2 + 0.67 NaCl$$
 (3)

$$Na_{0.67} [Li_{0.22}Mn_{0.78}]O_2 + 0.67 LiNO_3 \rightarrow Li_{0.67} [Li_{0.22}Mn_{0.78}]O_2 + 0.67 NaNO_3$$
 (4)

#### 2.4. Synthetic Control of the Intermediate

To further analyze the structure of the intermediate, we tried to prepare the pure intermediate via tuning various synthetic conditions, including Li/Na ratio, ball milling speed, the temperature etc. It is found that the formation of the pure intermediate is greatly hindered by the ion-exchange non-uniformity at the microscopic scale (micro/nano-meter level) and the metastable nature of the intermediate. Finally, a composite with the intermediate as the main phase (LLMO-M) was obtained by finely tuning the Li<sup>+</sup>/Na<sup>+</sup> exchange kinetics below room temperature (see details in Figure S9, Supporting Information). As shown in Figure 4A and Figure S9 (Supporting Information), the XRD pattern shows the strongest peak at ≈5.2 Å, corresponding to the intermediate phase. According to the percentage of the peak areas, the composite consists of 1% NLMO, 61% intermediate phase, 30% LLMO, and 8% Li<sub>2</sub>MnO<sub>3</sub>. Mn L-edge soft X-ray absorption spectrum (Figure S10, Supporting Information) of LLMO-M has a similar curve with those of NLMO and LLMO, hinting that, the ion-exchange process does not change the valence state of transition metal cations.

The local structure was examined by the electron diffraction map (Figure 4B) and the high-resolution TEM (HRTEM) image (Figure 4C). In Figure 4B, two sets of reflections are resolved by the line profile in the lower inset. The interlayer spacings can be deduced to 5.5 and 5.1 Å, respectively, according to the split peaks marked by the vertical black and red lines. They correspond to NLMO and the intermediate phase, respectively. It is consistent with the XRD result in Figure 4A. In addition, the intensity difference for two sets of reflections indicate that the dominant phase is the intermediate phase, which is also consistent with the XRD analysis in Figure 4A. In Figure 4C, HRTEM image presents the clear layered fringes with a spacing of ≈5.1 Å, confirming the formation of the layered intermediate phase. The reflections marked by the yellow arrows in the corresponding FFT map hint the spinel-like disordering. It indicates that, a certain amount of Mn cations migrate into the Li/Na layers during the ion-exchange process, which may benefit the cycling stability of the intermediate phase.

#### 2.5. Electrochemical Performance

16163028, 2023, 20, Downloaded from https://advanced.onlinelibrary.wiley.com/doi/10.1002/adfm.202214921 by University Town Of Shenzhen, Wiley Online Library on [23/11/2025]. See the Terms and Conditions (https://onlinelibrary.wiley.com/derm.

and-conditions) on Wiley Online Library for rules of use; OA articles are governed by the applicable Creative Commons License

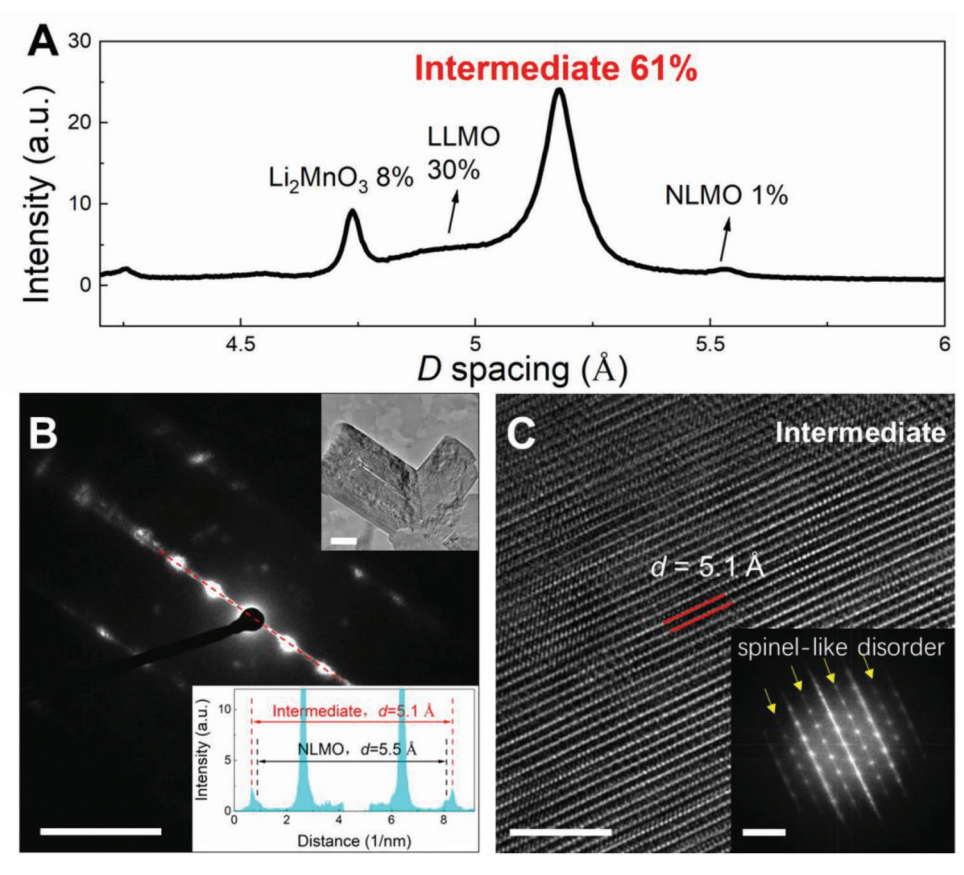


**Figure 4.** A) Selected-area XRD pattern of the composite with the intermediate phase as the main component. The selected *d* region is 4.2–6.0 Å from the full XRD pattern in Figure S9 (Supporting Information). B) The electron diffraction pattern from the selected primary particle (the upper inset). The scale bars in the pattern and the upper inset are 5 1/nm and 100 nm. The lower inset presents the line profile along the dashed red line. C) HRTEM image and the corresponding FFT map (inset) for the selected area. The scale bars in the image and inset are 5 nm and 5 1/nm.

undergoes a fast capacity decrease to  $\approx 230$  mA h g<sup>-1</sup> by the 10th cycle. LLMO-M delivers a moderate initial capacity of  $\approx 260$  mA h g<sup>-1</sup> and gradually degrades to  $\approx 220$  mA h g<sup>-1</sup> by the 10th cycle. The CV curves in the first five cycles were presented in Figure 5D–F. They all exhibit an oxidation peak above 4.5 V at the first charge and a pair of redox peaks at  $\approx 3$  V during repeated cycles, which come from O redox and Mn redox, respectively. Differently, the redox peaks of LLMO-MS are much sharper than those of LLMO-RT and LLMO-M, which may be due to the better crystallinity through the calcination, reflected by the narrower peak width in the corresponding XRD pattern (Figure S11, Supporting Information).

The rate performance of the three samples was also compared in Figure 4G. It is clear, the rate performance of LLMO-RT and LLMO-M is comparable to that of LLMO-MS. Figure 4H presents their cycling stability at 1 C. LLMO-MS shows a slow activation process from 34 to 155 mA h g $^{-1}$  in the first 100 cycles, and maintains the constant capacity in the 100th–160th cycle, then starts to degrade slowly. LLMO-RT has an activation process in the first five cycles with a higher initial capacity of  $\approx 175-190$  mA h g $^{-1}$ , then starts fast capacity degradation (62% after 200 cycles). LLMO-M has the highest initial capacity of 213 mA h g $^{-1}$  and no activation process. It undergoes a relatively fast capacity decrease in the first 50 cycles, and then maintains a superior cycling stability in the following cycles

(98% capacity retention from the 50th to the 200th cycle). The initial capacity decrease may be related to the impure phase components of Li<sub>2</sub>MnO<sub>3</sub>, the precursor and the final phase, while the excellent cycling stability should be related to the unique layered structure with a larger interlayer spacing and spinel-like cationic mixing in the intermediate phase. To explore the cause of the capacity decrease of LLMO-M, XRD pattern and HRTEM images of the LLMO-M electrode after 50 cycles at 1 C were collected. As shown in Figure S12 (Supporting Information), the superlattice peak of Li<sub>2</sub>MnO<sub>3</sub> in LLMO-M disappeared after 50 cycles, which indicated the structure degradation of Li<sub>2</sub>MnO<sub>3</sub>. As shown in Figure S13 (Supporting Information), LLMO-RT still maintains well layered structure, while a small amount of spinel-like lattice can be observed by the corresponding FFT maps. The spinel-like phase may come from the structure degradation of Li<sub>2</sub>MnO<sub>3</sub>. So, we can attribute the capacity decrease to the structure degradation of the impurity Li<sub>2</sub>MnO<sub>3</sub> partially. It is expected that better electrochemical performance can be achieved in the pure intermediate phase.

Overall, the cathodes prepared by mild conditions demonstrate an electrochemical performance comparable to that obtained by the high-temperature molten salt method, and perform even better in the initial capacity, reflecting the advantage of the low-temperature ion-exchange, especially in the energy efficiency and cost reduction.

1616308, 2023, 20, Downloaded from https://advanced.onlinelibrary.wiley.com/doi/10.1002/adfm.202214921 by University Town Of Shenzhen, Wiley Online Library on [23/11/2025]. See the Terms and Conditions

onditions) on Wiley Online Library for rules of use; OA articles are governed by the applicable Creative Commons License

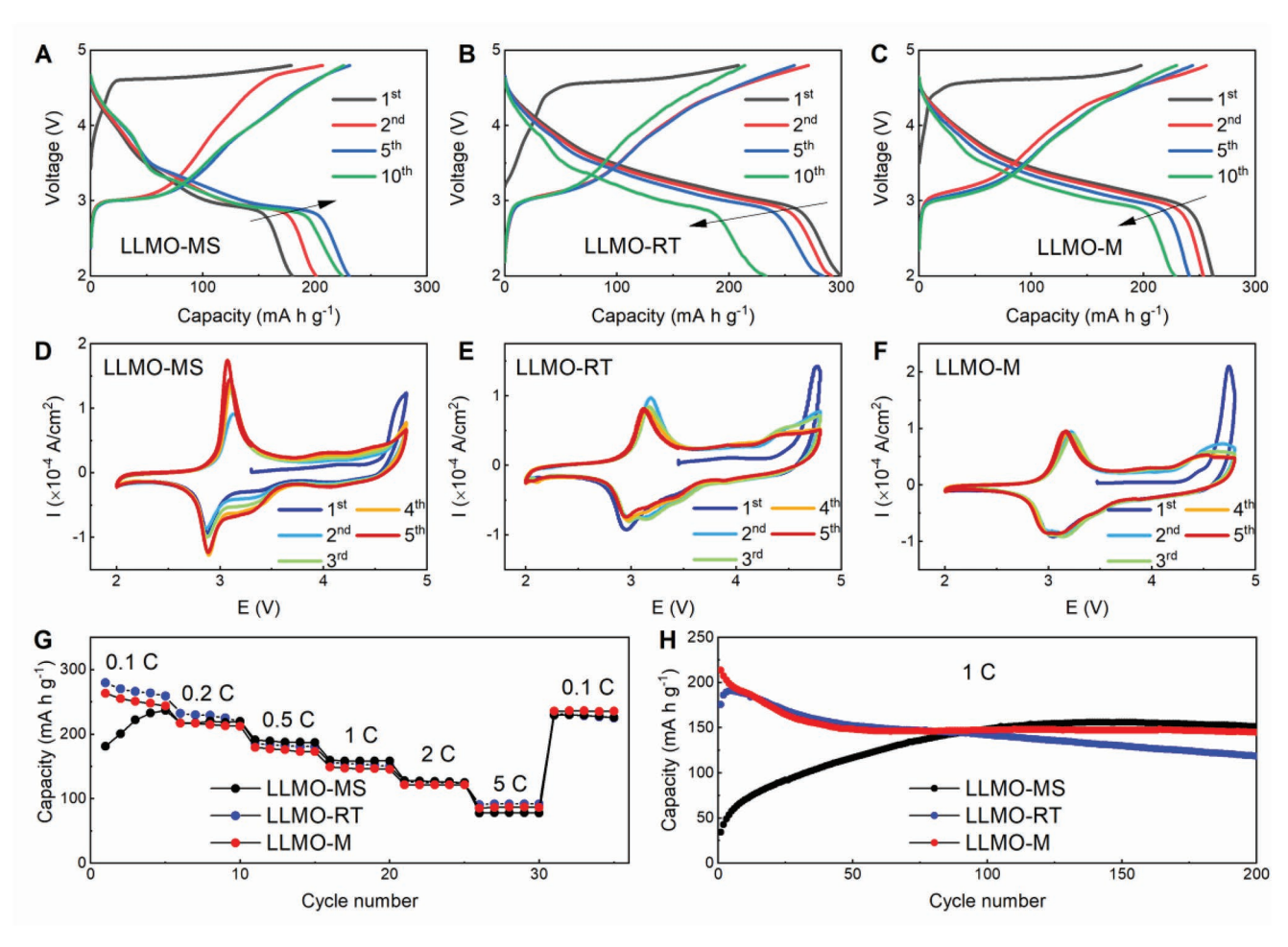


Figure 5. The selected charge-discharge profiles of A) LLMO-MS, B) LLMO-RT, and C) LLMO-M at 0.1 C. 1 C is set as 250 mA  $g^{-1}$ . The CV curves of D) LLMO-MS, E) LLMO-RT, and F) LLMO-M in the first five cycles at the scanning rate of 0.1 mV  $s^{-1}$ . G) The rate performance of LLMO-MS, LLMO-RT, and LLMO-M. H) The cycling performance of LLMO-MS, LLMO-RT, and LLMO-M at 1 C.

## 3. Conclusion

In conclusion, we combined in situ synchrotron XRD and DFT calculations to conduct the systemic studies into the structural changes during the ion-exchange process of an Mn-only layered cathode Li<sub>0.67</sub>[Li<sub>0.22</sub>Mn<sub>0.78</sub>]O<sub>2</sub>. The quantitative analysis revealed that the Li+/Na+ exchange reaction is favorable thermodynamically, and can be divided into two steps: 1) the first 60% of Li<sup>+</sup>/Na<sup>+</sup> exchange induces the 1st topotactic phase transformation from Na-containing precursor with a large interlayer spacing 5.55 Å to a layered intermediate phase with a medium interlayer spacing ≈5.16 Å; 2) the further ion exchange produce the final layered phase with a small interlayer spacing 4.88 Å through another topotactic phase transformation. Based on the understanding, an energy-efficient method of roomtemperature ball milling was developed to complete the ion exchange reaction, and an intermediate-dominant composite was obtained by slowing down the ion exchange kinetics below room temperature. The composite exhibits better electrochemical performance than the sample prepared by the traditional molten salt method. These findings embody the significance of synthetic kinetics in controlling material structure, and provide

vital guides for the preparation of high-performance Mn-based cathodes at mild conditions.

### 4. Experimental Section

Material Synthesis: First, the Na-containing precursor  $Na_{0.67}Li_{0.22}Mn_{0.78}O_2$  (NLMO) was prepared by a conventional solgel method. In a typical process, the stoichiometric amounts of  $Na(CH_3COO)\cdot 3H_2O$  and  $Mn(CH_3COO)\cdot 4H_2O$  with 10% excess  $Li(CH_3COO)\cdot 2H_2O$  were dissolved in the dilute nitric acid solution. Then a certain amount of polyvinyl pyrrolidone (PVP) was added as a chelating agent. Next, the mixed solution was evaporated to obtain a viscous gelunder vigorous stirring at 90 °C. The gel was dried at 140 °C for 3 h, and later annealed at 500 °C for 3 h to remove the organic constituents. Finally, the annealed powder was calcined at 700 °C for 10 h and slowly cooled down to form NLMO.

In a typical molten salt method for ion exchange, the NLMO sample was mixed with the molten salt LiNO $_3/\text{LiCl}$  (88:12 w/w) thoroughly in a weight ratio of 1:1 (equivalent to the Li $^+/\text{Na}^+$  molar ratio 2.136), and the mixture was heated at 280 °C for 6 h to complete the Li $^+/\text{Na}^+$  exchange. The powder was washed several times using deionized water, then dried at 80 °C overnight to obtain Li $_{0.67}\text{Li}_{0.22}\text{Mn}_{0.78}\text{O}_2$  (LLMO-MS).

In a room-temperature ball milling process for ion exchange, the NLMO sample was mixed with the molten salt LiNO<sub>3</sub>/LiCl (88:12 w/w)

thoroughly in a weight ratio of 1:1. Then the mixture was loaded with some  $ZrO_2$  balls in the canner for ball milling. The rotating speed was set to 200 rpm. A little amount of powder was extracted for XRD measurement at intervals to check the extent of ion exchange. The reaction was stopped until the XRD pattern did not change with time.

To obtain the intermediate phase, the NLMO powder was mixed with 0.1 m LiCl aqueous solution in a Li<sup>+</sup>/Na<sup>+</sup> molar ratio of 1:1 at 1.2 °C. The temperature was controlled by a ice-water bath. After stirring for 2 min, the powder was washed several times by deionized water and dried at 80 °C overnight.

In Situ High-Energy XRD Measurements: Temperature-resolved high-energy XRD patterns were collected from the mixture of NLMO and the molten salt mentioned above during calcination, at Sector 17–BM of the Advanced Photon Source (APS) at Argonne National Laboratory. The wavelength of the X-ray beam was 0.24099 Å. For in situ experiments, the mixture was pressed into pellets with a thickness of 1 mm and a diameter of 7 mm and loaded into a quartz tube, which was then placed in a Linkam 600 furnace perpendicular to the X-ray beam. The pellets were heated in air to 280 °C by 10 °C min<sup>-1</sup>, then maintained for 6 h, and cooled down to room temperature. During the calcination, a 2D X-ray detector was deployed to collect the XRD patterns at a rate of 2 scans min<sup>-1</sup>. The focused spot size was 0.5 mm (Horizontal) × 0.5 mm (Vertical).

Material Characterizations: Ex situ XRD patterns were collected from a Bruker D8-Advance diffractometer with Cu- $K\alpha$  radiation ( $\lambda$  = 1.5419 Å) at 45 kV and 100 mA. A Zeiss SUPRA-55 scanning electron microscope (SEM) was used to detect the morphology of the samples. Transmission electron microscopy was performed by an FEI TecnaiG2 F30 TEM microscope. The soft X-ray absorption spectroscopy (XAS) experiments for the Mn L edge were performed at beamline 02B02 of the SiP·ME2 platform, the Shanghai Synchrotron Radiation Facility (SSRF). The spectra were collected using surface-sensitive total electron yield (TEY) and bulk-sensitive total fluorescence yield (TFY) modes simultaneously at room temperature in an ultrahigh vacuum chamber.

DFT Calculations: First-principles calculations were performed based on the density functional theory (DFT) method as implemented in the Vienna ab initio simulation package (VASP).[20] The core electron contributions were described by the Projector augmented wave (PAW) potentials and the valance electrons were described by the planewave basis set with a cutoff energy of 520 eV.[21] The electronic energy convergence criterion was set at 10<sup>-6</sup> eV. The generalized gradient approximation (GGA) with the Perdew-Burke-Ernzerhof (PBE) functional was chosen as the exchange-correlation potential.<sup>[22]</sup> In all the calculations, the Brillouin zone was sampled by Monkhorst-Pack k-point grid with the density of 1000 per reciprocal atom. In order to correctly characterize the localization of transition-metal d electrons, The GGA+U method was used to remedy the strong correlation in the calculations.<sup>[23]</sup> The value for the Hubbard U parameter for Mn was 4.2 eV.[24] Geometries were optimized until the forces on the atoms were less than 0.02 eV  $Å^{-1}$ . The spin polarization was considered in all calculations. All calculations were performed considering a ferromagnetic ordering of Mn atoms.

The reaction enthalpies ( $\Delta H)$  are calculated according to the following equations.

$$\Delta H_1 = E(Li_{0.67}MnO_2) + 0.67E(NaCl) - E(Na_{0.67}MnO_2) - 0.67E(LiCl) \tag{5}$$

$$\Delta H_2 = E(Li_{0.67}MnO_2) + 0.67E(NaNO_3) - E(Na_{0.67}MnO_2) - 0.67E(LiNO_3)$$
 (6)

$$\begin{split} \Delta H_3 &= E \Big( \text{Li}_{0.67} \big[ \text{Li}_{0.22} \text{Mn}_{0.78} \big] \text{O}_2 \Big) + 0.67 E \big( \text{NaCl} \big) \\ &- E \Big( \text{Na}_{0.67} \big[ \text{Li}_{0.22} \text{Mn}_{0.78} \big] \text{O}_2 \Big) - 0.67 E \big( \text{LiCl} \big) \end{split} \tag{7}$$

$$\begin{split} \Delta H_4 &= E \Big( \text{Li}_{0.67} \big[ \text{Li}_{0.22} \text{Mn}_{0.78} \big] \text{O}_2 \Big) + 0.67 E \big( \text{NaNO}_3 \big) \\ &- E \Big( \text{Na}_{0.67} \big[ \text{Li}_{0.22} \text{Mn}_{0.78} \big] \text{O}_2 \Big) - 0.67 E \big( \text{LiNO}_3 \big) \end{split} \tag{8}$$

Electrochemical Measurements: Active materials, acetylene black carbon and polyvinylidene fluoride (PVDF) with a weight ratio of 8:1:1 were mixed thoroughly in N-methyl pyrrolidone (NMP) to obtain a well-mixed slurry.

Then the slurry was cast on the Al foil and dried at 110  $^{\circ}$ C in a vacuum oven overnight. Coin cells (CR2032) were assembled with lithium foil as the counter electrode and the polymer membrane (Celgard 2400) as the separator. The electrolyte was 1 M lithium hexafluorophosphate (LiPF<sub>6</sub>) solution in ethylene carbonate (EC) and ethyl methyl carbonate (EMC) in the volume ratio of 1:1. The as-assembled cells were charged and discharged in galvanostatic mode by NEWARE system. Cyclic voltammetry (CV, at the scan rate of 0.1 mV s<sup>-1</sup>) results were collected by a model CH1604E electrochemical workstation.

# **Supporting Information**

Supporting Information is available from the Wiley Online Library or from the author.

## Acknowledgements

B.C., Z.C., and H.C. contributed equally to this work. This work was financially supported by the National Natural Science Foundation of China (52172175), the Shenzhen Science and Technology Research Grant (JCYJ20210324130812033, JCYJ20200109140416788), the Chemistry and Chemical Engineering Guangdong Laboratory (1922018), the National Key R&D Program of China (2020YFB0704500), and the Major Science and Technology Infrastructure Project of Material Genome Big-science Facilities Platform supported by Municipal Development and Reform Commission of Shenzhen.

### **Conflict of Interest**

The authors declare no conflict of interest.

#### **Data Availability Statement**

The data that support the findings of this study are available in the supplementary material of this article.

#### **Keywords**

layered intermediate, Li<sup>+</sup>/Na<sup>+</sup> ion-exchanges, lithium-ion batteries, Mn-based layered cathodes, two-step phase transformations

Received: December 22, 2022 Revised: February 1, 2023 Published online: February 17, 2023

- [1] a) M. S. Whittingham, Chem. Rev. 2004, 104, 4271; b) V. Etacheri,
   R. Marom, R. Elazari, G. Salitra, D. Aurbach, Energy Environ. Sci. 2011, 4, 3243.
- [2] a) A. Boulineau, L. Croguennec, C. Delmas, F. Weill, Solid State Ionics 2010, 180, 1652; b) X. N. Liu, L. Z. Zhou, Q. J. Xu, Int. J. Electrochem. Sci. 2015, 10, 8899.
- [3] a) B. Cao, Y. Li, M. Zhang, N. Cheng, M. Shen, B. Hu, J. Li, Z. Li, S. Xu, W. Zhao, N. Yang, J. Sun, S. Dou, Y. Ren, H. Chen, L. Yin, F. Pan, J. Power Sources 2022, 551, 232148; b) J. L. Lu, B. Cao, B. W. Hu, Y. X. Liao, R. Qi, J. J. Liu, C. J. Zuo, S. Y. Xu, Z. B. Li, C. Chen, M. J. Zhang, F. Pan, Small 2022, 18, 2103499.
- [4] a) J. Xiao, X. Li, K. Tang, M. Long, J. Chen, D. Wang, H. Gao, H. Liu, Surf. Innov. 2022, 10, 119; b) V. Pimenta, M. Sathiya,



www.advancedsciencenews.com

SCIENCE NEWS\_\_\_\_\_



www.afm-journal.de

16163028, 2023, 20, Downloaded from https://advanced.onlinelibrary.wiley.com/doi/10.1002/adfm.202214921 by University Town Of Shenzhen, Wiley Online Library on [23/11/2025]. See the Terms

and Conditions

of use; OA articles are governed by the applicable Creative Commons

- D. Batuk, A. M. Abakumoy, D. Giaume, S. Cassaignon, D. Larcher, J.-M. Tarascon, *Chem. Mater.* **2017**, *29*, 9923.
- [5] a) X. H. Zhu, F. Q. Meng, Q. H. Zhang, L. Xue, H. Zhu, S. Lan, Q. Liu, J. Zhao, Y. H. Zhuang, Q. B. Guo, B. Liu, L. Gu, X. Lu, Y. Ren, H. Xia, Nat. Sustain. 2021, 4, 392; b) J. Billaud, R. J. Clement, A. R. Armstrong, J. Canales-Vazquez, P. Rozier, C. P. Grey, P. G. Bruce, J. Am. Chem. Soc. 2014, 136, 17243; c) P. He, H. J. Yu, D. Li, H. S. Zhou, J. Mater. Chem. 2012, 22, 3680.
- [6] A. R. Armstrong, P. G. Bruce, Nature 1996, 381, 499.
- [7] K. S. Kang, Y. S. Meng, J. Breger, C. P. Grey, G. Ceder, Science 2006, 311, 977.
- [8] Y. Zuo, B. Li, N. Jiang, W. Chu, H. Zhang, R. Zou, D. Xia, Adv. Mater. 2018, 30, 1707255.
- [9] X. Cao, H. F. Li, Y. Qiao, M. Jia, X. Li, J. Cabana, H. S. Zhou, Adv. Mater. 2021, 33, 2004280.
- [10] J. Song, B. Li, Y. Y. Chen, Y. X. Zuo, F. H. Ning, H. F. Shang, G. Feng, N. Liu, C. H. Shen, X. P. Ai, D. G. Xia, Adv. Mater. 2020, 32, 2000190.
- [11] a) D. Eum, B. Kim, S. J. Kim, H. Park, J. P. Wu, S. P. Cho, G. Yoon, M. H. Lee, S. K. Jung, W. L. Yang, W. M. Seong, K. Ku, O. Tamwattana, S. K. Park, I. Hwang, K. Kang, Nat. Mater. 2020, 19, 419; b) B. M. de Boisse, J. Jang, M. Okubo, A. Yamada, J. Electrochem. Soc. 2018, 165, A3630.
- [12] F. H. Ning, B. Li, J. Song, Y. X. Zuo, H. F. Shang, Z. M. Zhao, Z. Yu, W. S. Chu, K. Zhang, G. Feng, X. Y. Wang, D. G. Xia, *Nat. Commun.* 2020, 11, 4973.
- [13] a) W. Huang, L. Yang, Z. Chen, T. Liu, G. Ren, P. Shan, B. W. Zhang, S. Chen, S. Li, J. Li, C. Lin, W. Zhao, J. Qiu, J. Fang, M. Zhang, C. Dong, F. Li, Y. Yang, C. J. Sun, Y. Ren, Q. Huang, G. Hou, S. X. Dou, J. Lu, K. Amine, F. Pan, Adv. Mater. 2022, 34, 2202745;
  b) W. Huang, C. Lin, J. Qiu, S. Li, Z. Chen, H. Chen, W. Zhao, G. Ren, X. Li, M. Zhang, F. Pan, Chem 2022, 8, 2163; c) Y. Chen, Y. Liu, J. Zhang, H. Zhu, Y. Ren, W. Wang, Q. Zhang, Y. Zhang, Q. Yuan, G.-X. Chen, L. C. Gallington, K. Li, X. Liu, J. Wu, Q. Liu, Y. Chen, Energy Stor. Mater. 2022, 51, 756; d) X. Cao, J. Sun, Z. Chang, P. Wang, X. Yue, J. Okagaki, P. He, E. Yoo, H. Zhou, Adv. Funct. Mater. 2022, 32, 2205199; e) H. Shang, Y. Zuo, F. Shen, J. Song, F. Ning, K. Zhang, L. He, D. Xia, Nano Lett. 2020, 20, 5779; f) N. Yabuuchi, R. Hara, M. Kajiyama, K. Kubota, T. Ishigaki,

- A. Hoshikawa, S. Komaba, *Adv. Energy Mater.* **2014**, *4*, 1301453; g) J. M. Paulsen, R. A. Donaberger, J. R. Dahn, *Chem. Mater.* **2000**, *12*, 2257; h) X. Cao, H. Li, Y. Qiao, M. Jia, H. Kitaura, J. Zhang, P. He, J. Cabana, H. Zhou, *Sci. Bull.* **2022**, *67*, 381.
- [14] H. Gwon, S. W. Kim, Y. U. Park, J. Hong, G. Ceder, S. Jeon, K. Kang, Inorg. Chem. 2014, 53, 8083.
- [15] a) J. M. Paulsen, C. L. Thomas, J. R. Dahn, J. Electrochem. Soc. 2000, 147, 861; b) J. M. Paulsen, J. R. Dahn, J. Electrochem. Soc. 2000, 147, 2478; c) J. M. Paulsen, D. Larcher, J. R. Dahn, J. Electrochem. Soc. 2000, 147, 2862.
- [16] M. J. Zhang, Y. D. Duan, C. Yin, M. F. Li, H. Zhong, E. Dooryhee, K. Xu, F. Pan, F. Wang, J. M. Bai, Sci. Adv. 2020, 6, eabd9472.
- [17] a) W. Zhang, P. K. Liaw, Y. Zhang, Sci. China-Mat. 2018, 61, 2; b) A. Sarkar, Q. Wang, A. Schiele, M. R. Chellali, S. S. Bhattacharya, D. Wang, T. Brezesinski, H. Hahn, L. Velasco, B. Breitung, Adv. Mater. 2019, 31, 1806236; c) Z. Zheng, M.-Y. Weng, L.-Y. Yang, Z.-X. Hu, Z.-F. Chen, F. Pan, Chinese J. Struc. Chem. 2019, 38, 2020.
- [18] a) Y. Shin, W. H. Kan, M. Aykol, J. K. Papp, B. D. McCloskey, G. Chen, K. A. Persson, Nat. Commun. 2018, 9, 4597; b) X. Liu, G.-L. Xu, V. S. C. Kolluru, C. Zhao, Q. Li, X. Zhou, Y. Liu, L. Yin, Z. Zhuo, A. Daali, J.-J. Fan, W. Liu, Y. Ren, W. Xu, J. Deng, I. Hwang, D. Ren, X. Feng, C. Sun, L. Huang, T. Zhou, M. Du, Z. Chen, S.-G. Sun, M. K. Y. Chan, W. Yang, M. Ouyang, K. Amine, Nat. Energy 2022, 7, 808.
- [19] J. Lu, B. Cao, B. Hu, Y. Liao, R. Qi, J. Liu, C. Zuo, S. Xu, Z. Li, C. Chen, M. Zhang, F. Pan, Small 2022, 18, 2103499.
- [20] a) G. Kresse, J. Hafner, Phys Rev B Condens Matter 1993, 47, 558;
  b) G. Kresse, J. Furthmüller, Comp. Mater. Sci. 1996, 6, 15; c) G. Kresse,
  J. Furthmuller, Phys. Rev. B 1996, 54, 11169; d) S. K. Mishra, G. Ceder,
  Phys. Rev. B 1999, 59, 6120.
- [21] a) P. E. Blochl, Phys. Rev. B 1994, 50, 17953; b) G. Kresse, D. Joubert, Phys. Rev. B 1999, 59, 1758.
- [22] J. P. Perdew, K. Burke, M. Ernzerhof, Phys. Rev. Lett. 1996, 77, 3865.
- [23] a) S. L. Dudarev, G. A. Botton, S. Y. Savrasov, C. J. Humphreys,
   A. P. Sutton, *Phys. Rev. B* 1998, *57*, 1505; b) V. I. Anisimov, J. Zaanen,
   O. K. Andersen, *Phys. Rev. B* 1991, *44*, 943.
- [24] L. Wang, T. Maxisch, G. Ceder, Chem. Mater. 2007, 19, 543.